Wave boundary layer model in SWAN revisited

Jianting Du[1,3,4], Rodolfo. Bolaños[2], Xiaoli Guo Larsén[1], and Mark Kelly[1]

[1]Department of Wind Energy, Technical University of Denmark, Risø Campus, Roskilde, Denmark
[2]DHI, Agern Allé 5, DK-2970 Hørsholm, Denmark
[3]First Institute of Oceanography, Ministry of Natural Resources of China
[4]Laboratory for Regional Oceanography and Numerical Modeling, Qingdao National Laboratory for Marine Science and Technology, Qingdao, China

Correspondence: Jianting Du (dujt@fio.org.cn)

Abstract. In this study we extend the work presented in Du et al. (2017) to make the WBLM applicable for real cases by improving the wind input and white-capping dissipation source functions. Improvement via the new source terms includes three aspects. First, the WBLM wind-input source function is developed by considering the impact of wave-induced wind profile variation on the estimation of wave growth rate. Second, the white-capping dissipation source function is revised to be not explicitly dependent on wind speed for real wave simulations. Third, several improvements are made to the numerical WBLM algorithm, which increase the model's numerical stability and computational efficiency. The improved WBLM wind-input and white-capping dissipation source functions are calibrated through idealized fetch-limited and depth-limited studies, and validated in real wave simulations during two North Sea storms. The new WBLM source terms show better performance in the simulation of significant wave height and mean wave period than the original source terms.

1 Introduction

The accuracy of spectral ocean wave models depends on the forcing from wind, water level, currents, etc. It also depends on the source terms and numerical methods (Ardhuin, 2012). In deep water conditions, the source terms are reduced to wind-input source function (S_{in}), wave-breaking dissipation source function (S_{ds}), and nonlinear four-wave-interaction source function (S_{nl}). In a previous study (Du et al., 2017), a wave boundary layer model (WBLM) was implemented in the third generation ocean wave model SWAN (Booij et al., 1999) to improve the wind-input source function of Janssen (1991, hereafter JANS); this was done by considering the momentum and kinetic energy conservation at each level in the wave boundary layer. It was shown that the new S_{in} improves wave simulations in idealized fetch-limited conditions. Because the evolution of wave spectrum depends on the difference between source and sink terms, the change of S_{in} has to be followed by the tuning of the parameters in S_{ds} (Cavaleri, 2009). Du et al. (2017) simply re-calibrated the white-capping dissipation parameters of Komen et al. (1984, here after KOM) to be proportional to the WBLM S_{in} (Babanin et al., 2010), and wind speed at 10 m (U_{10}) (Melville and Matusov, 2002). Such a method works in idealized fetch-limited conditions when the winds do not change over time. However, in real cases, wind speed and direction vary in time. Also, wave-breaking is related to wave properties such as wave steepness, rather than explicitly depending on wind speed (e.g. G. J. Komen et al., 1994). Moreover, in coastal areas,

the bottom friction and depth-induced breaking dissipation become important and they influence the shape of wave spectrum. Consequently S_{in} and S_{ds} are also modified by the shallow-water effect. Therefore the description of the new S_{in} and S_{ds} in shallow water also needs to be investigated, before they are used in real simulations.

Theoretical models of wave-breaking dissipation have been extensively reviewed by G. J. Komen et al. (1994), Young and Babanin (2006a), and Cavaleri et al. (2007) and can be classified into: white-capping models (Hasselmann, 1974), saturation-based models (e.g. Phillips, 1985), probabilistic models (e.g. Longuet-Higgins, 1969; Yuan et al., 1986; Hua and Yuan, 1992), and turbulent models (Polnikov, 1993). Among them, white-capping and saturation-based models are widely used in ocean wave models such as WAM (Komen et al., 1994), SWAN (Booij et al., 1999), WAVEWATCH III (Tolman and Chalikov, 1996), and MIKE 21 SW (Sørensen et al., 2004). White-capping models consider the effect of downward-moving whitecaps doing work against the upward-moving waves. Parameterization of white-capping dissipation can be found in e.g Komen et al. (1984), Bidlot et al. (2007), and Bidlot (2012); the dissipation at all frequencies is taken to be proportional to the mean wave steepness defined by a mean wave number and the significant wave height. The saturation-based models assume saturation exists in the equilibrium range of the wave spectrum, and the dissipation rate is proportional to the saturation at any given frequency. Therefore, the dissipation at each frequency is proportional to the local wave steepness or local saturation. Latter studies, however, suggest a two-phase behavior of wave-breaking dissipation (Babanin and Young, 2005; Young and Babanin, 2006a): S_{ds} should be a function of the spectral peak plus a cumulative frequency-integrated term at higher frequencies due to dominant wave-breaking. Considering the complexity of wave-breaking processes, recent studies tend to combine the two types of S_{ds} together. Alves and Banner (2003) and van der Westhuysen et al. (2007) used a saturation-based model multiplied by a KOM-shaped model, to account for the long-wave-short-wave and wave-turbulence interactions. Banner and Morison (2010) introduced a breaking probability function to the saturation-based model of Phillips (1985). Ardhuin et al. (2010), Babanin et al. (2010), and Zieger et al. (2015) added a cumulative term to a saturation-based model. Such combined S_{ds} are proved to be robust in wave simulations, globally to coastal areas (Ardhuin et al., 2012; Ardhuin and Roland, 2012; Leckler et al., 2013).

However, as more physical processes are being taken into account, expressions of S_{ds} become more complex and need more tuning parameters; e.g. the S_{ds} of Ardhuin et al. (2010) needs up to 18 parameters, which makes it difficult to adjust when there is modification of other source terms. The present study aims at finding a proper dissipation source function that is suitable for the new WBLM S_{in}. Therefore, instead of introducing more physics into S_{ds}, numerical adjustment is applied to the KOM dissipation (Komen et al., 1984). The reason that we chose the KOM S_{ds} is that it has been shown successful when used with different wind-input source functions in SWAN (Snyder et al., 1981; Komen et al., 1984; Janssen, 1991; Larsén et al., 2017), and because the formulation is such flexible that its total magnitude and spectral distribution can be easily tuned with C_{ds} and Δ in equation 12. Du et al. (2017) has shown that numerical adjustment to the KOM S_{ds} can be used for the WBLM S_{in}, to reproduce the fetch-limited wave growth curve of Kahma and Calkoen (1992). Moreover, Ardhuin (2012) showed that S_{ds} of the KOM type and saturation-based type (Phillips, 1985) can be adjusted to give very similar behavior. However, we found that using only the KOM S_{ds} within the WBLM produces too high energy level at frequencies higher than the spectral peak ($f > f_p$), and this problem can be solved by using a cumulative dissipation term according to Ardhuin et al. (2010).

In this paper, the improvement of WBLM S_{in}, the revised S_{ds}, and the numerical algorithm changes to the model are presented in section 2. Then the new pair of S_{in} and S_{ds} is calibrated in idealized fetch-limited and depth-limited study, and validated in real case storm simulations in the North Sea. These numerical experiments are described in section 3. And the results are presented in section 4. Wave parameters such as significant wave height, mean period, peak wave period, and spectral shape are validated using point measurements of deep and shallow waters. S_{in} and S_{ds} of KOM and JANS are also examined as benchmark reference for these storms. As mentioned before, wave growth depends on the difference between source and sink terms as well as numerical discretization methods, especially in real cases. Therefore it is difficult to distinguish whether an improvement of a specific wave parameter, such as significant wave height, is due to the improvement of S_{in} or S_{ds}. An evaluation of the WBLM S_{in} was presented in Du et al. (2017) in an idealized fetch-limited wave growth study, where the wave growth rate and the drag coefficient calculated from S_{in} are compared with measurements. However, this paper mainly focus in the application of WBLM for real applications, so that the overall effect of the new WBLM S_{in} and S_{ds} is emphasized.

2 Methods

2.1 The wind-input source function

According to Du et al. (2017), the growth rate (β_g) of the WBLM wind-input source function ($S_{in} = \beta_g(\sigma,\theta) N(\sigma,\theta)$) is expressed as:

$$\beta_g(\sigma,\theta) = C_\beta \sigma \frac{\tau_t(z)}{\rho_w c^2} cos^2(\theta - \theta_w), \tag{1}$$

where $N(\sigma,\theta)$ is the action density spectrum, θ and θ_w is the wave and wind direction, C_β is the Miles' parameter (Miles, 1957), ρ_w is the water density, and c is the phase velocity of waves. $\tau_t(z)$ is the local turbulent stress, which equals to the total stress, τ_{tot}, minus the wave-induced stress, $\tau_w(z)$. The Miles' parameter C_β is described as a function of the non-dimensional critical height, λ:

$$C_\beta = \frac{J}{\kappa^2} \lambda \ln^4 \lambda, \lambda \leq 1, \tag{2}$$

where $\kappa = 0.41$ is the von Kármán constant, and $J = 1.6$ is a constant. In Du et al. (2017), the expression of the non-dimensional critical height λ for Miles' parameter (equation 2) is derived by the assumption of a logarithmic wind profile followed Janssen (1991), and it is expressed as:

$$\lambda = \frac{g z_0}{c^2} \exp\left[\frac{\kappa}{(u_*/c + \alpha) \cdot \cos(\theta - \theta_w)}\right], \tag{3}$$

where g is the gravity acceleration, $\alpha = 0.008$ is a wave age tuning parameter according to Bidlot (2012), z_0 is the roughness length. However, it is found that using equation (3) causes numerically instability in some cases. This is because within the WBL, the wind profile is not logarithmic under the impact of waves (Du et al., 2017). Using a logarithm wind profile (equation 3) not only slows down the computation but could also fails in converging in some cases. Therefore when applying WBLM

S_{in}, the expression of λ also needs to be changed to adjust to the new wind profile. Here we follow Miles (1957)'s procedure to drive an approximate expression for λ. In Miles (1957) the non-dimensional critical height is defined as:

$$\lambda = kz_c, \tag{4}$$

where k is the wave number, z_c is the critical height where the wave phase velocity (c) equals the wind speed component in the phase velocity direction $u(z_c) \cdot \cos(\theta - \theta_w)$,

$$c = u(z_c) \cdot \cos(\theta - \theta_w), \tag{5}$$

5 where $\theta - \theta_w$ is the angular separation between wind and wave directions. We assume that in the vicinity of the critical height (z_c), the wind profile can be approximately described as locally logarithmic

$$\frac{du}{dz} = \frac{u_*^l}{\kappa z}, \tag{6}$$

where $u_*^l = \sqrt{\tau_t/\rho_a}$ is the local friction velocity. In the vicinity of the critical height, wind speed at any other heights z can be expressed as

$$u(z) = \frac{u_*^l}{\kappa} \ln(z) + z_0^l, \tag{7}$$

where z_0^l is a local effective roughness. Introducing equation (7) to equation (5), we have wind speed at the critical height

$$u(z_c) = \frac{c}{\cos(\theta - \theta_w)} = \frac{u_*^l}{\kappa} \ln(z_c) + z_0^l. \tag{8}$$

10 The critical height is calculated by combining equation (7) and (8)

$$z_c = z \cdot \exp\left[\frac{\kappa}{(u_*^l/c) \cdot \cos(\theta - \theta_w)} - \frac{\kappa u(z)}{u_*^l} \right]. \tag{9}$$

Considering the shallow water dispersion relation, $k = (g/c^2)\tanh(kh)$ with h the water depth, the combination of equation (4) and (9) results in the non-dimensional critical height for any direction

$$\lambda = kz_c = \frac{gz}{c^2} \tanh(kh) \cdot \exp\left[\frac{\kappa}{(u_*^l/c) \cdot \cos(\theta - \theta_w)} - \frac{\kappa u(z)}{u_*^l} \right]. \tag{10}$$

It is found that equation (10) tends to underestimate wave growth at low frequencies. We used the same method as that used in WAM (Bidlot, 2012), added a wave age tuning parameter $\alpha = 0.011$ to shift the wave growth towards lower frequencies:

$$\lambda = \frac{gz}{c^2} \tanh(kh) \cdot \exp\left[\frac{\kappa}{(u_*^l/c + \alpha) \cdot \cos(\theta - \theta_w)} - \frac{\kappa u(z)}{u_*^l} \right]. \tag{11}$$

15 ## 2.2 White-capping dissipation source function

The white-capping dissipation expression of KOM (Komen et al., 1984; Janssen, 1991; Bidlot et al., 2007) in SWAN is written as:

$$S_{ds}(\sigma, \theta) = -C_{ds} \langle\sigma\rangle \left(\langle k\rangle^2 m_0 \right)^2 \left[(1 - \Delta)\frac{k}{\langle k\rangle} + \Delta\left(\frac{k}{\langle k\rangle}\right)^2 \right] \phi(\sigma, \theta), \tag{12}$$

where $\phi(\sigma,\theta) = \sigma N(\sigma,\theta)$ is the frequency spectra. Since the WBLM wind-input and dissipation source functions are designed mainly for the wind sea, it is necessary to reduce the swell impact to the white-capping dissipation. In this study, the mean radian frequency $\langle\sigma\rangle$ and mean wave number $\langle k\rangle$ is modified according to Bidlot et al. (2007) to put more emphasis on the high frequencies

$$
\begin{cases}
\langle\sigma\rangle = \iint \sigma\phi(\sigma,\theta)\,d\theta d\sigma/m_0 \\
\langle k\rangle = \left[\iint k^{1/2}\phi(\sigma,\theta)\,d\theta d\sigma/m_0\right]^2,
\end{cases}
\tag{13}
$$

5 where $m_0 = \iint \phi(\sigma,\theta)\,d\theta d\sigma$ is the variance of the sea surface elevation. The choice of the two dissipation parameters, C_{ds} and Δ, are different for different wind-input source functions. For example, for KOM S_{in}, $C_{ds} = 2.5876$, $\Delta = 1$; for JANS S_{in}, $C_{ds} = 4.5$, $\Delta = 0.5$; for WBLM S_{in} in Du et al. (2017), $\Delta = 0.1$, and C_{ds} in S_{ds} is related to S_{in} to make sure

$$
\int S_{ds}(\sigma)\,d\sigma = R_{ds}\int S_{in}(\sigma)\,d\sigma,
\tag{14}
$$

where

$$
R_{ds} = 1 - 0.15\left(\frac{10}{U_{10}}\right)^{0.5} \cdot \max\left[1.0, 1.53\left(\frac{5.2\times10^{-7}}{\widetilde{E}}\right)^{0.25}\right],
\tag{15}
$$

where U_{10} is wind speed at 10 m, $\widetilde{E} = m_0 g^2/U_{10}^4$ is a non-dimensional energy. As discussed in the introduction, a dissipation
10 parameter that is strongly dependent on wind speed as in equation (15) only works in idealized fetch-limited cases but will in principle not work in real cases because wave breaking depends on wave state rather than wind. Here we explore the use of some wave parameters to replace U_{10} and S_{in} in equations (14) and (15) to get rid of the direct dependence on wind speed. We derive the relationship between U_{10}, m_0, peak frequency (f_p), and fetch (x) from the three non-dimensional parameters, namely non-dimensional energy ($\widetilde{E}$), non-dimensional peak frequency ($\widetilde{F}_p = f_p U_{10}/g$), and non-dimensional fetch ($\widetilde{x} = xg/U_{10}^2$). The
15 fetch dependence of $\widetilde{E}$ and $\widetilde{F}_p$ can be written as:

$$
\begin{cases}
\widetilde{E} = A\widetilde{x}^B \\
\widetilde{F}_p = C\widetilde{x}^D,
\end{cases}
\tag{16}
$$

where in Kahma and Calkoen (1992) (composite condition), $A = 5.2\times10^{-7}$, $B = 0.9$, $C = 2.1804$, $D = -0.27$. According to equation 16, U_{10}, $\widetilde{E}$, and $\widetilde{x}$ can be expressed as functions of m_0, f_p, and g:

$$
\begin{cases}
U' = \left[\frac{C^B}{A^D}\frac{m_0^D}{f_p^B}g^{2D+B}\right]^{\frac{1}{4D+B}} \\
E' = m_0 g^2/U'^4 \\
x' = (E'/A)^{1/B},
\end{cases}
\tag{17}
$$

where U_{10}, $\widetilde{E}$, and $\widetilde{x}$ are replaced by U', E', and x' since they are parameterized variables. The dissipation coefficient C_{ds} in equation (12) can be obtained by fitting the C_{ds} calculated from equation (14) and (15) with U' and x' from equation (17):

$$
C_{ds} = F(x', U').
\tag{18}
$$

The form and parameters in equation (18) will be obtained in the fetch-limited study in section 4.1. To increase the robustness of the wave modeling in case of unusual shaped spectra, the peak frequency f_p in equation (17) is replaced by $0.866\langle f\rangle$ according to Komen et al. (1994) who uses $k_p = 0.75\langle k\rangle$, where $\langle f\rangle = \langle\sigma\rangle/2\pi$ is the mean frequency. The use of $\langle f\rangle$ may cause uncertainty in estimating f_p, especially in e.g. bimodal wave cases. Considering the model performs quite well during the two storm simulations in section 4.3, during which bimodal waves probably exists, we assume that this uncertainty is relatively small.

To reduce the energy level at high frequencies, a cumulative term is added to the dissipation source functions. The cumulative dissipation term (S_{ds}^c) follows Ardhuin et al. (2010), but the directional dependence of dissipation rate is not considered:

$$S_{ds}^c(f,\theta) = -1.44 \times C_{cu}\phi(f,\theta)\int_0^{r_{cu}f}\max\left[\left(\sqrt{B(f')}-\sqrt{B_r}\right),0\right]^2|c-c'|'\,df',\tag{19}$$

where $C_{cu} = 1.0$ is a dissipation parameter, $B_r = 0.0012$ is a saturation threshold, $r_{cu} = 0.5$ is the ratio of the maximum frequency where dissipation of long waves influence short waves, C_g is the group velocity, $B(f)$ is the local saturation (van der Westhuysen et al., 2007):

$$B(f) = \int_0^{2\pi}k^3\cos^2(f,\theta')\phi(f,\theta')\frac{C_g}{2\pi}d\theta'.\tag{20}$$

2.3 Improvement on the numerical algorithm

Considering the expensive cost of WBLM code in Du et al. (2017), improvement on the numerical algorithm of the WBLM (Du et al., 2017) was done in the following aspects.

– Reducing the unnecessary calculations in the high frequencies. The WBLM uses 10 Hz as the maximum frequency, which is only being used for very young waves. Usually, the WBLM does not have to solve such high frequencies when the energy is so small that their contribution to the total wave-induced stress is negligible. Therefore, in the new code, the WBLM only solves the active frequency range which is dynamically changing with the wave spectrum. Although the maximum frequency is dynamically changing, all the active frequencies are solved, so there is no influence to the result. Such an adjustment reduces approximately half of the computation time in the idealized fetch-limited study in section 3.1.

– The standard calculation in SWAN, a sweeping technique is used for the directional propagation of the waves, which needs four times sweep for each time step. Such sweep is not necessary for the calculation of WBLM because the WBLM has to integrate over all directions of the spectrum. Therefore, WBLM only calculates once per time step.

With the above mentioned refinement, the WBLM is now about 5 times faster than the previous version in Du et al. (2017). It is still slower than KOM and JANS, but it is fast enough for real applications. The averaged calculation time during an idealized

fetch-limited study is list in table 1, including KOM, JANS, the previous WBLM of Du et al. (2017) (WBM Old), and the new WBLM in this paper. All the setups are same as Section 3.1, except JANS uses frequency number ranges from 38 to 54 for different wind speed conditions, while the other schemes use 73 frequencies.

Table 1. The calculation time of KOM, JANS, the previous WBLM of Du et al. (2017) (WBM Old), and the New WBLM during the idealized fetch-limited study.

Scheme	KOM	JANS	WBLM Old	WBLM New
Time (minutes)	184	151	975	217

3   Experiments

3.1   Idealized fetch-limited study

The revised dissipation parameter (equation 18) in S_{ds} together with the new non-dimensional critical height as in WBLM S_{in} were first calibrated in the idealized fetch-limited wave growth experiments with the same model setup as in Du et al. (2017). Here we briefly describe the model setup. We use the one-dimensional SWAN. The fetch is between 0 and 3000 km, with the spatial resolution changes gradually from 0.1 km to 10 km. The wave spectrum ranges from 0.01 to 10.51 Hz, and the frequency discretization was logarithmic with a frequency exponent of 1.1, which result in 73 frequencies. We use 36 directional bins with a constant spacing of $10°$. SWAN initializes from zero spectrum and runs for 72 h with a time step of 1 min. U_{10} ranges from 5 to 40 ms^{-1} and keeps constant during the 72 hours simulation.

The calibration process is carried out in three steps. Step 1, we run the model using the white-capping dissipation parameter as in Du et al. (2017) (equation 14 and 15) in the idealized fetch-limited study. Since we added a cumulative dissipation source term, the parameters in equation 15 has to be changed into equation 21 so as to best fit to the Kahma and Calkoen (1992) fetch-limited wave growth curves

$$R_{ds} = 1 - 0.18 \left(\frac{10}{U_{10}} \right)^{0.3} \cdot \max \left[1.0, 1.53 \left(\frac{5.2 \times 10^{-7}}{\widetilde{E}} \right)^{0.25} \right]. \tag{21}$$

In Step 2, the real form and parameters in equation 18 will be obtained by analyzing and fitting the C_{ds} with x' and U', which are calculated in Step 1. Finally, the best fit in Step 2 may not be the best choice for the wave model. Therefore, we selected several representative fitting parameters out of dozens of groups through idealized fetch-limited study as the final choice.

3.2   Idealized depth-limited study

In addition to the idealized fetch-limited study, the revised WBLM source terms are also tested in depth-limited wave growth experiments, to check if the new source terms perform well with the interaction of the other source terms in the wave model, including the bottom friction and depth-induced wave breaking dissipation source functions. Following SWAN (2014), we use

JONSWAP (Hasselmann et al., 1973) bottom friction with a bottom friction coefficient, $C_b = 0.038 \text{ m}^2\text{s}^{-3}$, and Battjes and Janssen (1978) depth-induced wave breaking source function with a breaker parameter, $\gamma = 0.8$.

In the depth-limited wave growth experiments, we take the measurements of Young and Babanin (2006b) as reference for validation, because they not only provided detailed wind, wave, and water depth information, but also provided wave spectrum
5   measurement from capacitance wave probes up to 10 Hz (Young et al., 2005). Zijlema et al. (2012) did similar depth-limited wave growth experiments for the calibration of the bottom friction parameter in SWAN, but they did not compare the wave spectrum. Zijlema et al. (2012) selected 10 representative cases from the data presented in Young and Babanin (2006b). We add 3 more cases because the wave spectrum in these three cases are also presented in Young and Babanin (2006b). This ends up with 13 cases in all, which are number 1, 11, 17, 23, 28, 30, 32, 58, 61, 63, 82, 83, and 87 in Table 1 of Young and Babanin
10   (2006b). Among them, number 1, 11, 28, 32, and 87 have wave spectrum records for model validation. In all the 13 cases, the water depth ranges from 0.89 m to 1.1 m, and the wind speed ranges from 5.7 ms^{-1} to 15 ms^{-1}. The fetch is set to 20 km with a spatial resolution of 0.1 km to ensure the fetch is long enough, and the wave growth is limited by the water depth. The frequency and directional discretization are same as the fetch-limited study. SWAN initializes from zero spectrum and runs for 24 h (we found 24 h is long enough for the wave development in the shallow water conditions in this study), with a time step
15   of 1 min. Two pair of S_{in} and S_{ds} are tested, namely KOM (Snyder et al., 1981; Komen et al., 1984) and the revised WBLM in this study.

3.3   Real case study in the North Sea

The new WBLM S_{in} and S_{ds} are validated during two winter storms in the North Sea. Wind and wave measurements are obtained during the "Reducing the uncertainty of near-shore wind estimations using wind lidars and mesoscale models" (RUNE)
20   Project (Floors et al., 2016b). Simultaneous wind and wave measurements from lidar and buoy are available from Nov. 2015 to Jan. 2016. The experiment was conducted at the west coast of Jutland, Denmark, with an average water depth of 16.5 m. Details about the wind and wave measurements can be found in (Floors et al., 2016b, a, c; Bolaños, 2016; Bolaños and Rørbæk, 2016). Beside the standard wave parameters such as significant wave heights, peak wave period, and mean wave periods, the two-dimensional wave spectrum $E(f, \theta)$ are also available, which allows us to validate more detailed aspects of the
25   source functions. During the RUNE period, two storms passed the measurement site from 2015-11-28 to 2015-12-08. Wave simulations were done during this period with the three pair of source terms (KOM, JANS, and WBLM). Beside the measurement from the RUNE project, point wave measurements at Fjaltring, Hanstholm, A121, Vaderoarna, and Helgoland North from NOOS (https://noos.bsh.de/); FINO-1 and FINO-3 from FINO (http://fino.bsh.de) at; and Sleipner-A and Ekofisk from eKlima (http://sharki.oslo.dnmi.no) during the simulation period are also used for model validation. The locations of these
30   measurement sites are shown in Figure 1a, b and c.

SWAN is forced by the NCEP Climate Forecast System version 2 (CFSR) 10 m wind. The quality of CFSR 10 m wind speed and direction is evaluated with measurements in Figure 6a and 6b, and it has been shown to be good quality for wave simulations in the North Sea in many previous studies (Bolaños et al., 2014). Therefore, the hourly CFSR data may be considered reasonable wind forcing. Though it may not be accurate in the presence of highly fluctuating wind on scales smaller than 1 hour, e.g. Larsén
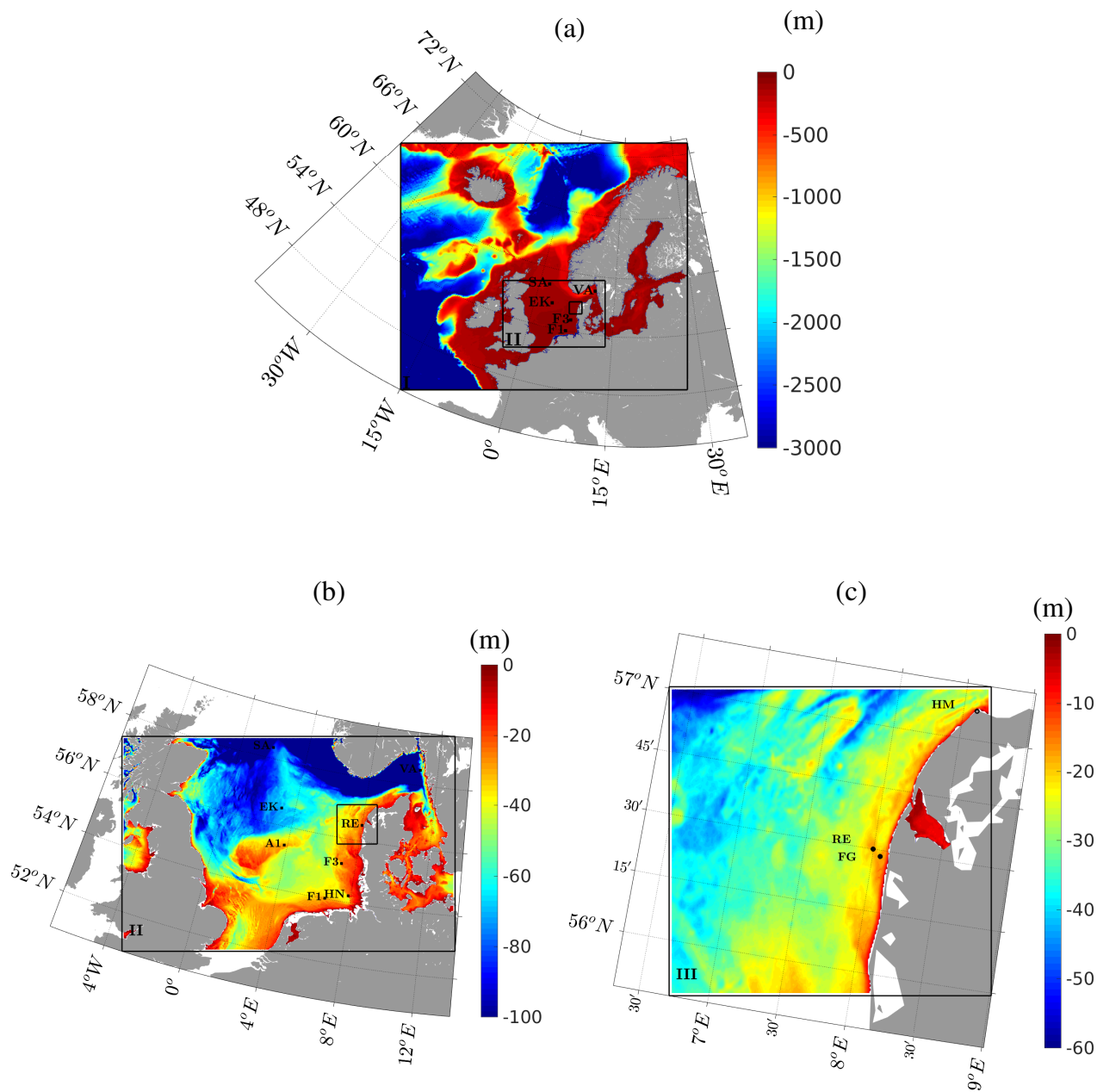
Figure 1. SWAN domain for RUNE storm simulation, with domain I 9 km resolution, II 3 km resolution, and III 600 m resolution. (a), (b), and (c) show the bathymetry at domain I, II, and III. Bathymetry are interpolated from EMODnet Digital Terrain Model (DTM) 1/8 arc-minute data. The 5 measurement sites, RUNE (RE), Fjaltring (FG), Hanstholm (HM), A121 (A1), Vaderoarna (VA), Helgoland North (HN), Fino-1 (F1), Fino-3 (F3), Sleipner-A (SA), and Ekofisk (EK), are shown as black dots.

et al. (2017). SWAN uses three nested domain, with a resolution downscaling from 9 km to 3 km and 600 m (Figure 1a). Open boundaries for SWAN are set to zero. The shortest fetch of the observation points is larger than 1000 km according to the wind direction during the storm. According to the fetch-limited study in section 4.1, the fetch is long enough for the waves to develop. The bottom friction and depth-induced wave breaking source functions for the real case study are same as the depth-limited

5   wave growth studies. Bathymetry data is obtained from the EMODnet Digital Terrain Model (DTM) with a spatial resolution of 1/8 arc-minute. Note that most of the observations are located in the coastal areas in the North Sea, except Sleipner-A, A121, and Ekofisk (Figure 1b and 1c). The water depth of the most sites are less than 30 m, except Sleipner-A and Ekofisk are relatively deeper, with water depth around 80 m and 60 m respectively. SWAN initializes from zero spectrum and the first 24 hours output are not included in our analysis. The first storm peak is about 72 hours after the model initialize to make sure the

10   duration of the simulation is long enough. The frequency discretization was logarithmic with a frequency exponent of 1.1, and the lowest frequency was set to 0.03 Hz. For KOM and WBLM source terms, a cut-off frequency of 10.05 Hz is used, giving a total number of 61 frequencies; for JANS source terms, the cut-off frequency is set to 0.57 Hz to make sure the simulation stable, giving a total number of 31 frequencies. We used 36 directional bins and 5 min time step. A summary of the constants and model setups used for all the experiments in section 3 are listed in Table 2 and Table 3, respectively.

Table 2. Constants used for all the experiments in section 3. C_{ds} and Δ are white-capping dissipation parameters in equation (12); $F(x', U')$ is the new dissipation parameter for WBLM in equation (18); C_{cu}, B_r, and r_{cu} are cumulative dissipation parameter for WBLM in equation (19); C_b and γ are JONSWAP (Hasselmann et al., 1973) bottom friction and Battjes and Janssen (1978) depth-induced wave breaking parameters.

	C_{ds}	Δ	C_{cu}	B_r	r_{cu}	$C_b (m^2 S^{-3})$	γ
KOM	2.5876	1.0	–	–	–	0.038	0.8
JANS	4.5	0.5	–	–	–	0.038	0.8
WBLM	$F(x', U')$	0.1	1.0	0.0012	0.5	0.038	0.8

Table 3. A summary of model setups for all the experiments in section 3. dx is the spatial resolution and dt is the time step of SWAN in seconds.

Experiments	Simulation time	$U_{10}(\text{ms}^{-1})$	Bathymetry	dx (km)	dt (sec)	Frequency (Hz)	Direction bins
Fetch-Limitted	72 h	5.0 - 40	5000 m	0.1 - 10	60	0.001 - 10.51	36
Depth-Limitted	24 h	5.7 - 15	0.89 - 1.1 m	0.1	60	0.001 - 10.51	36
RUNE storms	2015-11-28 to 2015-12-08	CFSR	EMODnet DTM	9-3-0.6	300	0.003 - 10.05 (0.57 for JANS)	36

4 Results

4.1 Idealized fetch-limited study

The significant wave height (H_{m0}) calculated from Step 1 of the idealized fetch-limited study using equation 14 and 21 are shown in Figure 2a. The Kahma and Calkoen (1992) wave growth curves are also shown as solid black lines for reference. Note that Kahma and Calkoen (1992) curves come from data with limited wind speeds ($U_{10} \leq 25$ ms^{-1}) and fetches ($x \leq 300$ km), and we linearly extend them to broader ranges. The H_{m0} calculated from Step 1 (solid colored lines in Figure 2a) agree with Kahma and Calkoen (1992) wave growth curves for fetches $x \leq 10$ km. But it tends to underestimate H_{m0} for fetches $x > 10$ km. Therefore, in Step 2 we only fit the C_{ds} in the first 10 km and extend its application for longer fetches. The C_{ds} calculated from Step 1 for wind speed $U_{10} = 5$ ms^{-1} and $U_{10} = 20$ ms^{-1} are shown in Figure 2b as black circles and black rectangles. Here we try to speculate the form of equation 18 based on the distribution of C_{ds} from Step 1 in Figure 2b. First, C_{ds} has a clear dependence on U_{10}. We found that in 10 ms^{-1} wind speed condition, the simulated H_{m0} follows the Kahma and Calkoen (1992) curves quite well in all fetches, while in the other wind speed conditions, the model underestimates H_{m0} when $U_{10} < 10$ ms^{-1} or overestimates H_{m0} when $U_{10} > 10$ ms^{-1}. Therefore, we take 10 ms^{-1} as reference, and there should be a $\left(\frac{U'}{10}\right)$ term in the C_{ds} equation. Second, C_{ds} depends on the fetch, considering the fetch dependence is logarithmic (the horizontal coordinate of Figure 2b is logarithmic), there should be a $ln(x)$ term in the C_{ds} equation. Considering that a log transformed quantity must be unitless, we use the non-dimensional fetch $ln(x')$ instead of $ln(x)$. Therefore, we assume C_{ds} in equation 18 has the following form:

$$C_{ds} = [C1 \cdot \ln^{C2}(x') + C3] \cdot \left(\frac{U'}{10}\right)^{C4}, \tag{22}$$

where $C1$, $C2$, $C3$, and $C4$ are parameters to be determined by fitting the C_{ds} calculated from Step 1. Directly use the four parameters maybe easier to fit, but it requires more effort to use or change it in real applications. Therefore, instead of finding a random combination of the four parameters who gives the least square error, we prefer to reduce the number of fitting parameters based on our understanding of the role of the two terms, namely $ln(x')$ and $\left(\frac{U'}{10}\right)$ in equation 22. We use fixed value for the power on $ln(x')$ and $\left(\frac{U'}{10}\right)$. By testing $1 \leq C2 \leq 4$ with a resolution of 1, and $0 \leq C4 \leq 1$ with a resolution of 0.1, we choose $C2 = 2$ and 4, $C4 = 0.5$ and 1 as representative values. With the values of $C2$ and $C4$ provided, we fit $C1$ and $C3$ with the data from Step 1 and end up with the first 3 groups of fitting parameters listed in Table 4 (FIT1 to FIT3). FIT4 in Table 4 is an improvement for FIT3 which will be described latter. The fitted C_{ds} using FIT1 to FIT4 at different wind speed conditions are shown in Figure 2b as colored lines with circles and rectangles representing wind speed.

The 4 groups of parameters (FIT1 to FIT4 in Table 4) are applied in SWAN in the fetch-limited study, and the results are shown in Figure 2c and 2d. The effect of the $\left(\frac{U'}{10}\right)^{C4}$ term in equation 22 can be seen from the comparison between FIT1 and FIT2. The fitted C_{ds}, simulated H_{m0} and f_p of FIT1 and FIT2 are shown in Figure 2b, 2c, and 2d as blue solid and red solid lines with circles and rectangles representing wind speed. Although significant difference of C_{ds} between $C4 = 1.0$ (FIT1) and $C4 = 0.5$ (FIT2) is seen in Figure 2b, the resulted H_{m0} and f_p show relatively small difference. In low wind speed conditions ($U_{10} = 5$ and 10 ms^{-1}), $C4 = 1.0$ (blue solid lines in Figure 2c and 2d) results in larger H_{m0} (smaller f_p) than $C4 = 0.5$

Table 4. Four groups of fitting parameters (FIT1, FIT2, FIT3, FIT4) for equation 22.

	$C1$	$C2$	$C3$	$C4$
FIT1	30.74	4	1.169	1.0
FIT2	83.61	4	1.605	0.5
FIT3	13.08	2	1.241	0.5
FIT4	23.02	1.41255	0.0	0.0

(red solid lines in Figure 2c and 2d). In high wind speed conditions ($U_{10} = 20$ and 40 ms^{-1}), $C4 = 1.0$ underestimates H_{m0} (overestimates f_p) more than $C4 = 0.5$ in long fetches ($x > 10$ km).

   The effect of the $ln(x')^{C2}$ term can be seen from the comparison between FIT2 and FIT3, the red solid and magenta dashed lines in Figure 2b, 2c, and 2d. The impact of $C2$ to H_{m0} and f_p is much weaker than $C4$. Using $C2 = 2$ (magenta dashed lines

5 in Figure 2c and 2d) results in slightly larger H_{m0} (smaller f_p) than $C2 = 4$ (red solid lines in Figure 2c and 2d) in long fetches ($x > 10$ km), which results in larger white-capping dissipation, smaller H_{m0}, and larger f_p.

   FIT1-FIT3 tend to underestimate H_{m0} (overestimates f_p) in long fetches ($x > 10$ km). In the real case study in section 4.3, it will be shown that such an underestimation of H_{m0} failed in capturing large waves in real storm simulations. Therefore, we continuously reduce the value of $C2$ and $C4$ until the large waves are captured in both idealize fetch-limited study and real case

10 study, which results in the parameters of FIT4 (hereafter WBLM). In FIT4, $C4 = 0.0$ means that $\left(\frac{U'}{10}\right)$ term is disappeared in equation 22. From equation 17 we found that both U' and x' could be written in the form of $A_1 m_0^{A_2} f_p^{A_3}$, which indicate that the function of U' term could be replaced by changing the parameters in x' term. This can be seen from the green lines in Figure 2b that, without $\left(\frac{U'}{10}\right)$ term C_{ds} still follows different curve in different wind speed condition.

   Figure 3a shows the wave spectrum from WBLM (solid lines) in 10 ms^{-1} wind speed condition after 72 h simulation in

15 comparison with the spectrum parameterization of D85 (Donelan et al., 1985) (dashed lines) and JONSWAP (Hasselmann et al., 1973) (doted lines) with the fetch dependence from Kahma and Calkoen (1992). Detailed equations for D85 and JONSWAP are listed in Appendix A. The results from WBLM source term generally follows the shape of the D85 and JONSWAP spectrum, but it tends to underestimate the energy at low frequencies at fetches $x \geq 10$ km. The D85 spectra at short fetches (e.g. 1 km) has less energy in high frequencies (e.g. $f > 1$ Hz) than in long fetches (e.g. 3000 km). On the contrary, JONSWAP and

20 WBLM spectrum have more energy in short fetches than long fetches in high frequencies. The D85 spectra has a f^{-4} shape at high frequencies, while JONSWAP has a f^{-5} shape. The high frequency part of WBLM spectra is between f^{-4} and f^{-5}. Figure 3b shows the source term distribution of wind-input (S_{in}, solid lines), white-capping dissipation (S_{ds}, dashed lines), and 5 times cumulative dissipation ($5S_{ds}^c$, doted lines) source functions at different fetches indicated by color legends in Figure 3a. $5S_{ds}^c$ instead of S_{ds}^c is used to better visualize the cumulative dissipation source term. As the waves grow older, the S_{in}

25 in high frequencies become smaller, and S_{ds}^c become larger, which may explain why the WBLM spectra has more energy in short fetches than in long fetches in high frequencies. Figure 3c shows the corresponding stress distribution within the wave boundary layer. Here we also use $5\tau_w^l$ (doted lines) instead of τ_w^l for the purpose of visualizing the local wave-induced stress. Short fetch waves contribute more surface stress than long fetch waves in high frequencies, while they contribute less stress
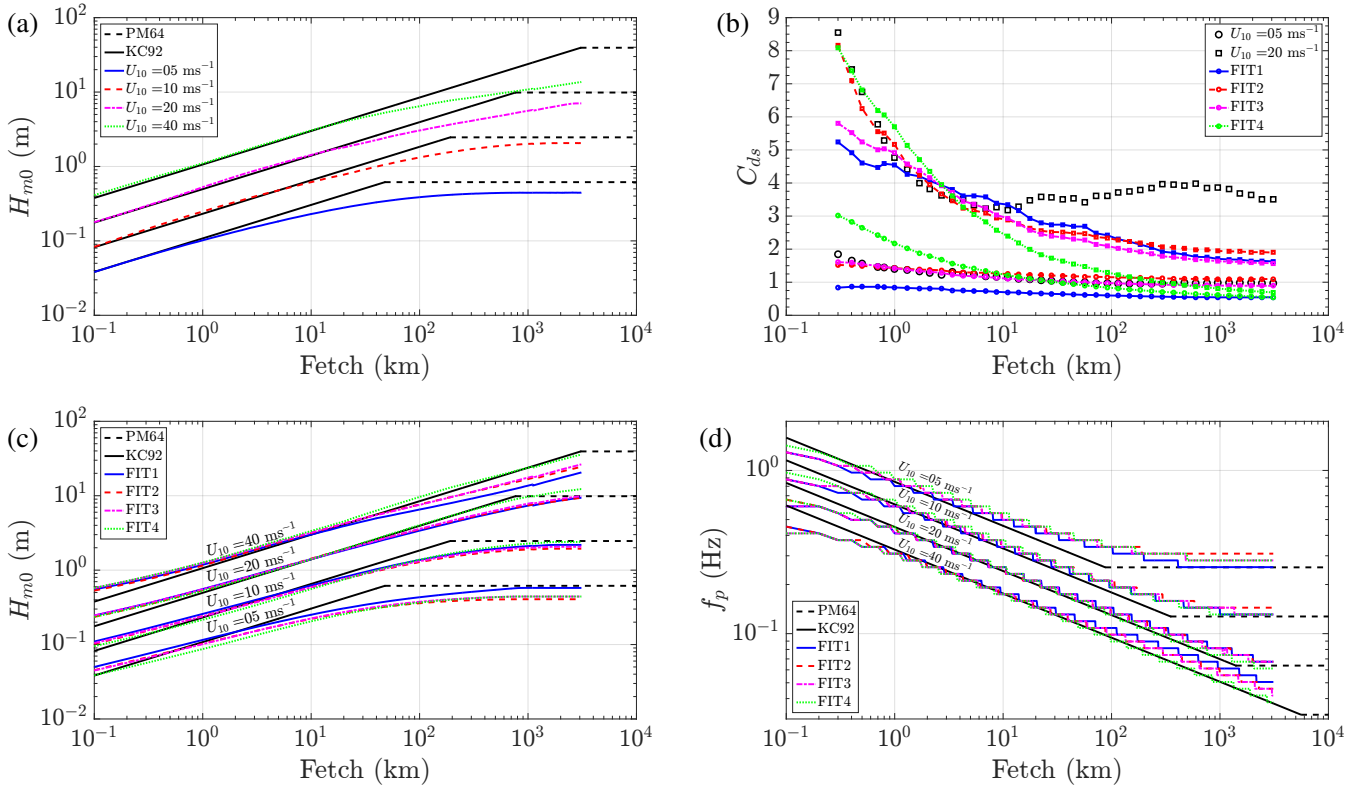
Figure 2. H_{m0} as a function of fetch after 72 hours of simulation in different wind speed condition using equation 21 as the white-capping dissipation parameter (panel a). C_{ds} as a function of fetch after 72 hours of simulation in different wind speed condition using equation 21, and fitted C_{ds} using FIT1 to FIT4 (panel b). H_{m0} and f_p as a function of fetch using white-capping dissipation parameters from FIT1 to FIT4 (panel c and d).

than long fetch waves in low frequencies. The total wave-induced stress depend on the integration of τ_w^l at all frequencies, which results in waves with fetch of 5 - 15 km have the highest total wave-induced stress, waves with fetch of 1 km have lower total wave-induced stress, and waves with fetch of 3000 km have the lowest wave-induced stress. Accordingly, total wind stress (τ_{tot}, thick solid lines) at 5 - 15 km is larger than 1 km and 3000 km because of the impact of the waves. Figure

5 3d shows the wind profiles within the wave boundary layer calculate by WBLM. Wind profiles are rather different in different wave development stage, which reveals that it is necessary to take the wave-induced wind profile variation into account in the estimation of the critical height in section 2.1.

4.2 Idealized depth-limited study

Figure 4 shows the non-dimensional wave energy as a function of non-dimensional depth for fully developed waves in shallow

10 waters after 24 h simulation, with the measurements of Young and Babanin (2006b) as reference. In comparison, results from
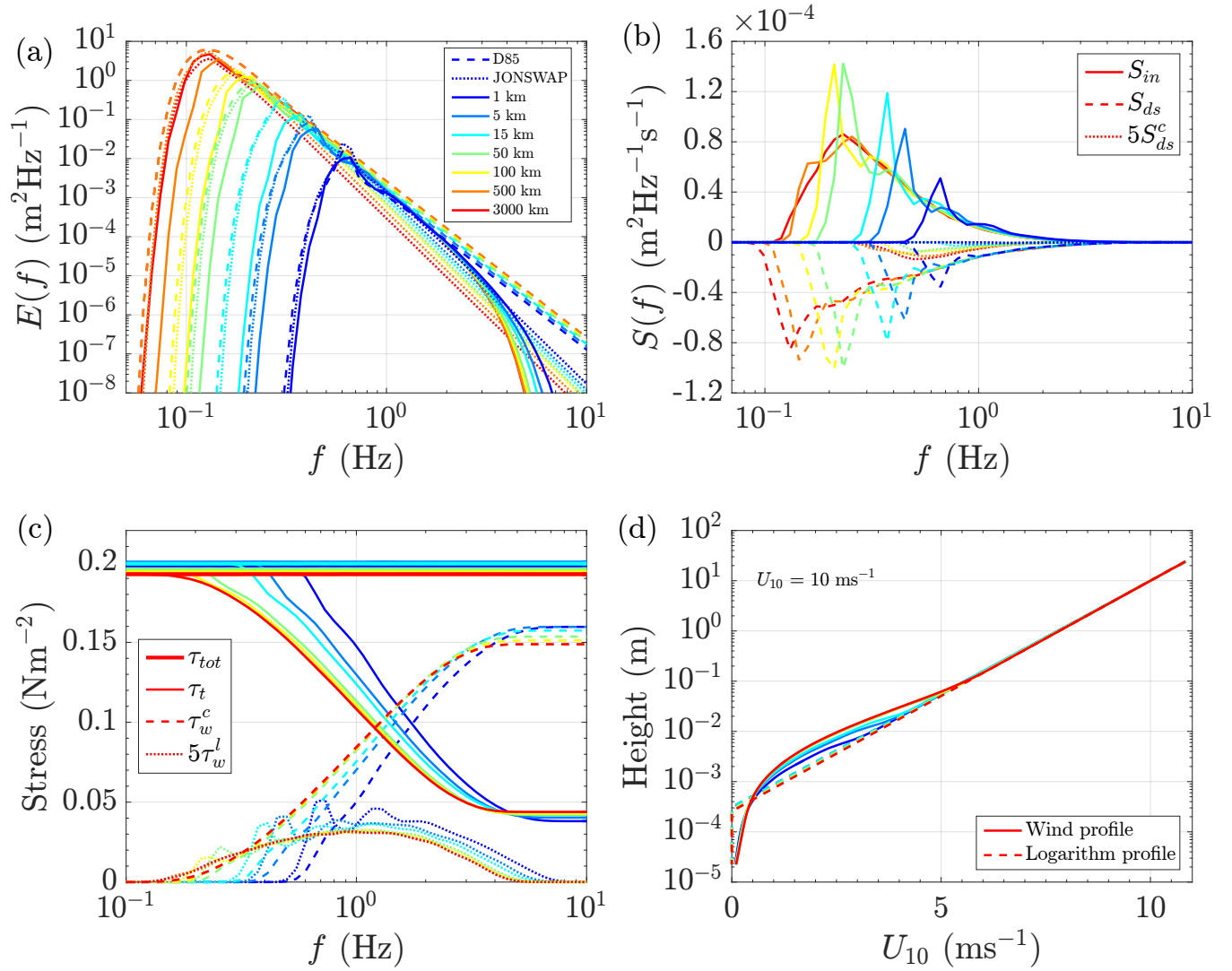
Figure 3. Wave spectrum (a), wind-input and dissipation source terms (b), stress distribution over frequencies (c), and wind profile (d) calculated from WBLM, in 10 ms^{-1} wind speed condition at different fetches after 72 h simulation, in the fetch-limited wave growth study. The dashed lines and doted lines in panel (a) are the wave spectrum parameterization from D85 (Donelan et al., 1985) and JONSWAP (Hasselmann et al., 1973), the solid lines are from WBLM. The solid, dashed, and doted lines in panel (b) are the WBLM wind-input (S_{in}), white-capping dissipation (S_{ds}), and 5 times cumulative dissipation ($5S_{ds}^c$) source functions, respectively. Thick solid, thin solid, dashed, and doted lines in panel (c) are the total stress (τ_{tot}), turbulent stress (τ_t), cumulative wave-induced stress (τ_w^c), and 5 times local wave-induced stress ($5\tau_w^l$) from WBLM. The solid lines in panel (d) are calculated from WBLM, and the dashed lines are the relative logarithm wind profiles extended from wind speed at 10 m elevation.

KOM source terms are also shown. Both of the WBLM (red crosses) and KOM (blue squares) show close agreement with the measurements (black circles).

The one-dimensional wave spectrum in the depth-limited experiment is further examined after 24 h simulation in Figure 5a-e for different wind speed and depth conditions, with the measurements of Young and Babanin (2006b) as reference. Both models capture the peak of the wave spectrum. However, KOM (blue lines) tends to underestimate the energy level at high frequencies. On the contrary, the energy level of WBLM (red lines) at high frequencies closely follows the measurements.
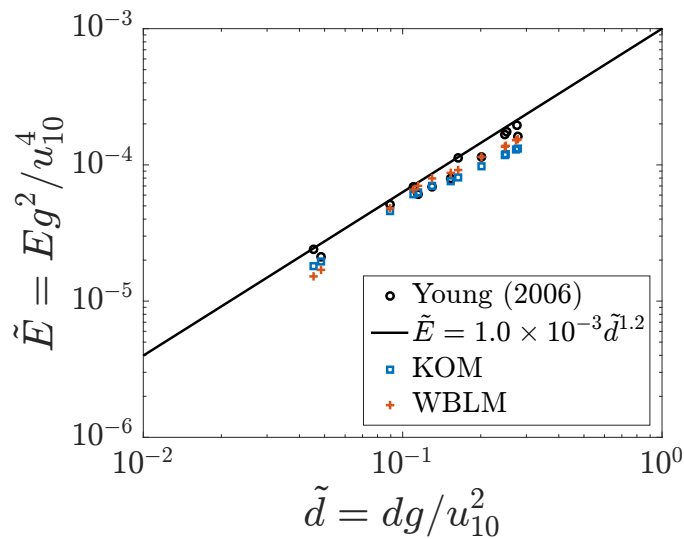
Figure 4. Observed (black circles) and parameterized (black line) non-dimensional wave energy for fully developed waves in shallow water as a function of non-dimensional depth (Young and Babanin, 2006b) and SWAN results with KOM (blue squares)and WBLM (red crosses) source terms after 24 h simulation.

4.3 Two storms during RUNE project

During the two RUNE storms from 2015-11-28 to 12-08, wave simulation was done with SWAN forced by CFSR wind. The performance of KOM, JANS, and WBLM source terms are evaluated with buoy measurements in terms of significant wave height H_{m0}, mean wave direction D_{mean}, peak period T_p, mean period T_{m01}, and one-dimensional wave spectrum. Figure 6 shows the simulated time series of H_{m0}, D_{mean}, T_p, and T_{m01} in comparison with buoy measurements at RUNE. To see the impact of different parameters of the WBLM white-capping dissipation source function to the wave simulation, results from FIT1 to FIT3 are also shown. Similar to the conclusions in the idealized fetch-limited study in section 4.1, these parameters significantly underestimate high waves. Only FIT4 (here WBLM) can be used for real wave simulations to capture the high waves.

Now we compare the performance of the new WBLM with KOM and JANS source terms. For H_{m0}, D_{mean}, and T_p, all the modeled time series generally follow the general trends of measurement data. The biggest error of H_{m0} happens at the
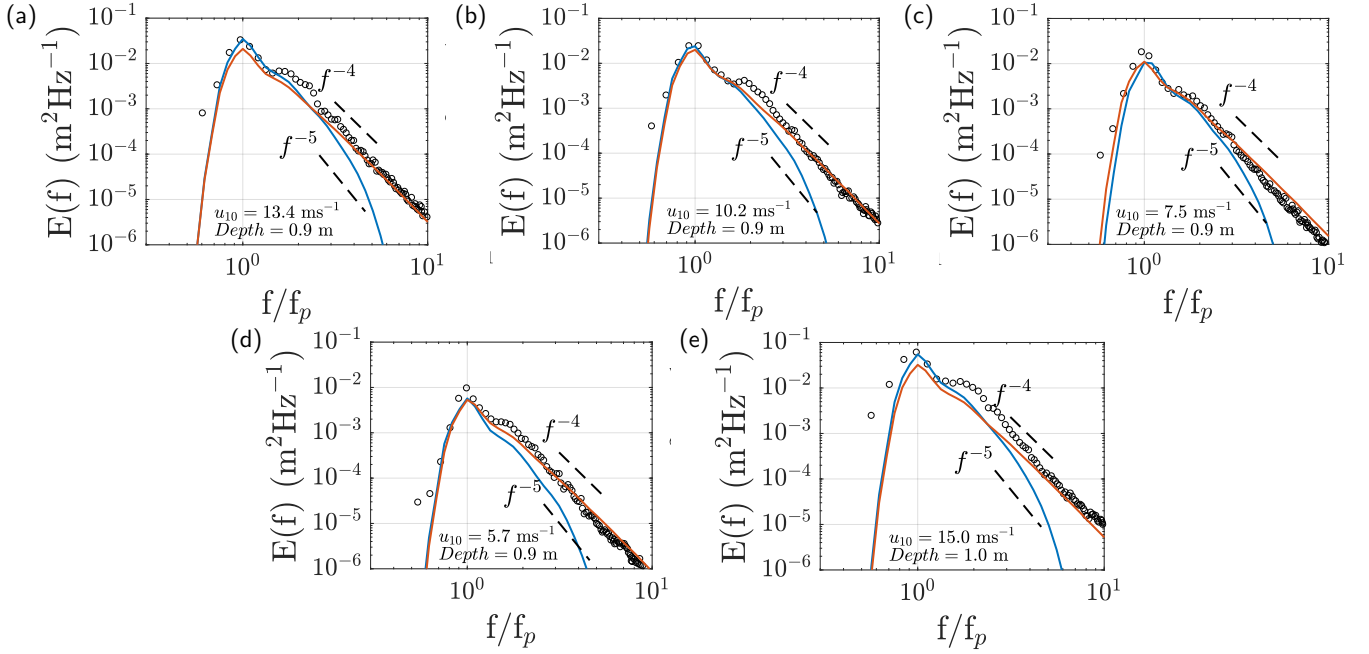
Figure 5. One dimensional wave spectrum measured by (Young and Babanin, 2006b) (black circles) for fully developed waves in shallow water and the results from SWAN with KOM (blue lines) and WBLM (red lines) source functions after 24 h simulation.

two storm peaks. The three source terms overestimate the H_{m0} during the peak about 1 m (15%). WBLM gives slightly better H_{m0} during the peak than KOM and JANS. But it tends to underestimate T_p during the storm peaks. WBLM predicts T_{m01} significantly better than KOM and JANS. Note that the Buoy T_{m01} is calculated from the frequency range of 0.005 Hz to 0.64 Hz, JANS is from 0.03 Hz to 0.58 Hz, KOM and WBLM is from 0.03 Hz to 0.63 Hz. A summary of the statistics is listed in Table 5, and the definition of the statistics are given in Appendix B. WBLM generally gives better result for H_{m0} and T_{m01} than KOM and JANS. All the three source terms give similar accuracy in predicting D_{mean}. WBLM is slightly less accurate in predicting T_p than KOM and JANS.

Table 5. Statistics of simulated significant wave height (H_{m0}), mean wave direction (D_{mean}), and peak (T_p) and mean (T_{m01}) wave period in comparison with buoy measurements at RUNE site from 2015-11-28 to 2015-12-08. The statistics include mean difference (BIAS), root mean square difference (RMSE), and scatter index (SI). In each column, the values of smallest absolute errors are signed with bold text.

Exp.	$H_{m0}(m)$			D_{mean} (°)			$T_p(s)$			T_{m01}		
	BIAS	RMSE	SI	BIAS	RMSE	SI	BIAS	RMSE	SI	BIAS	RMSE	SI
KOM	0.24	0.62	0.18	3.99	**8.32**	**0.03**	0.25	**1.24**	**0.13**	1.60	1.74	0.11
JANS	**0.17**	**0.52**	0.15	3.40	8.74	**0.03**	0.23	1.36	0.14	1.56	1.71	0.11
WBLM	0.35	**0.52**	**0.12**	2.98	8.84	**0.03**	-0.13	1.44	0.15	**0.57**	**0.67**	**0.06**
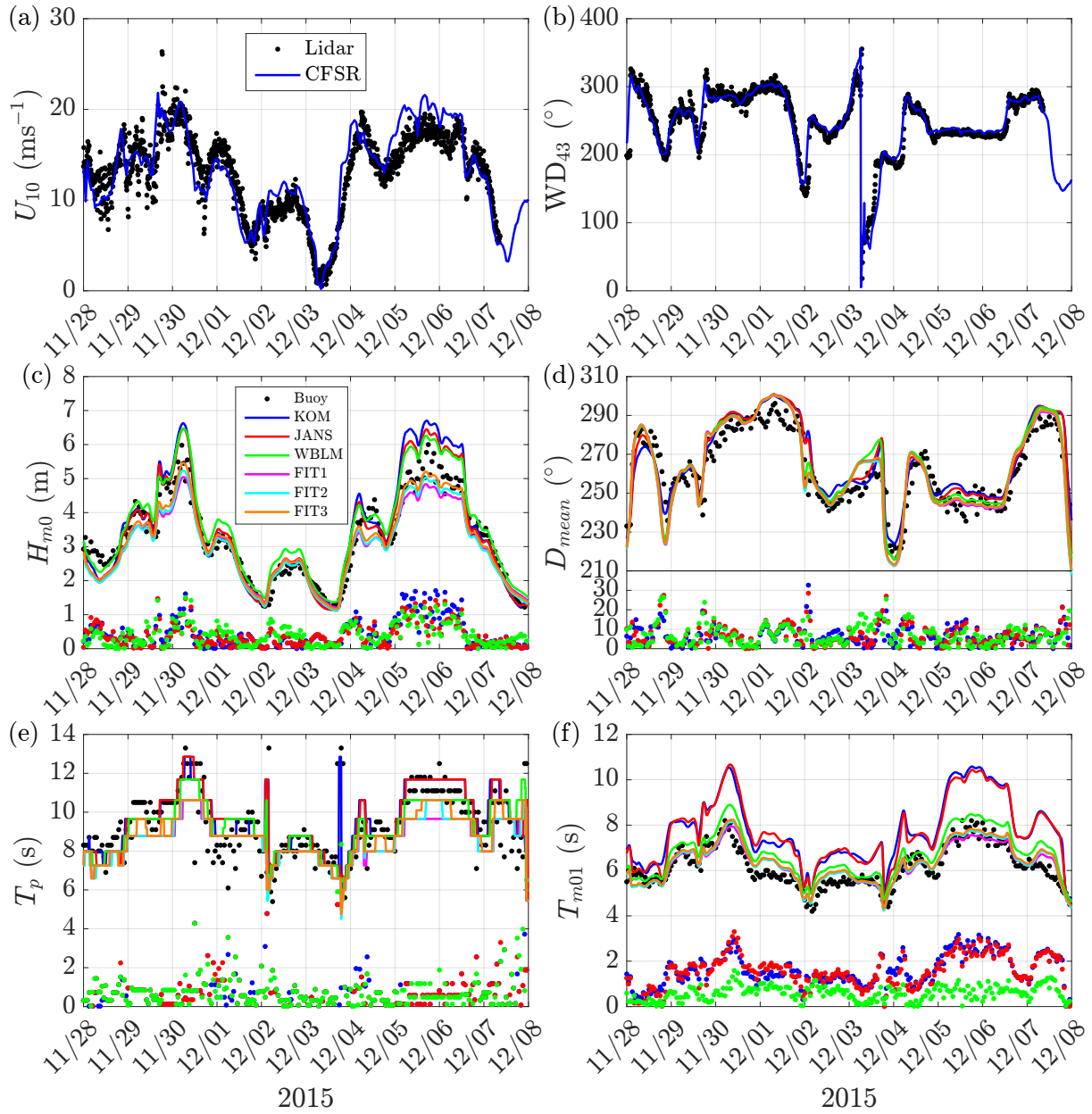
Figure 6. Time series during two winter storms in RUNE project. (a). 10 m wind speed from CFSR and measurements calculated from a logarithm wind profile from Lidar measurements at 43 m, 50 m, 62 m, 82 m, and 100 m. (b). Wind direction from CFSR and Lidar measurement at 43 m. (c). Modeled significant wave height (solid lines) in comparison with Buoy measurement (black dotes), colored dotes show the absolute error. (d). Mean wave direction. (e). peak wave period. (f). mean wave period.

The time series of H_{m0} at another 9 measurement sites, including Fjaltring (FG), Hanstholm (HM), A121 (A1), Vaderoarna (VA), Helgoland North (HN), Fino-1 (F1), Fino-3 (F3), Sleipner-A (SA), and Ekofisk (EK) in the North Sea during the two storm simulation are shown in Figure 7. The relative statistics are listed in Table 6. Considering the statistics of mean difference (BIAS), root mean square difference (RMSE), and scatter index (SI), WBLM generally gives better H_{m0} than KOM and JANS

5   for most of the sites. However in contrast to RUNE, WBLM tends to underestimate the largest waves during storm peaks in the open ocean sites, e.g. the storm peak at A121 (Figure 7c), Sleipner-A (Figure 7g), and Ekofisk (Figure 7i).
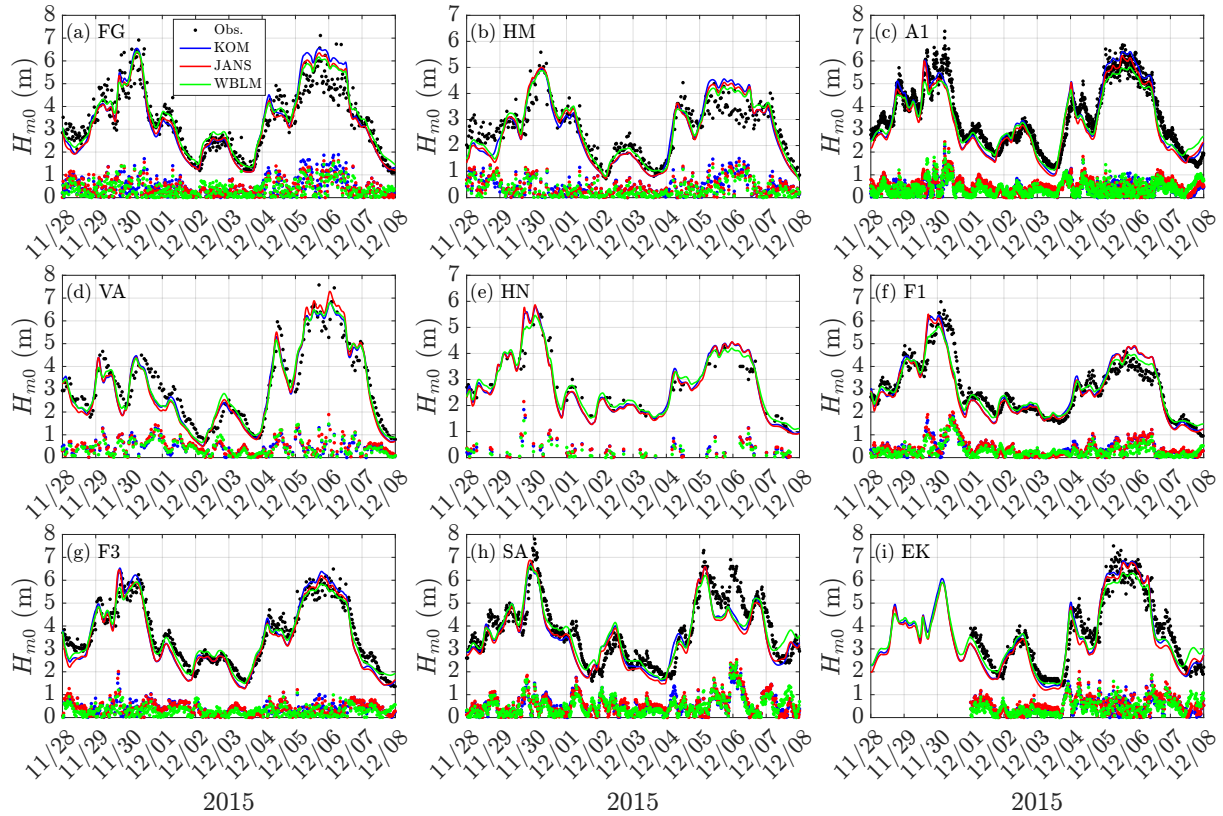
Figure 7. Time series of H_{m0} at Fjaltring (FG), Hanstholm (HM), A121 (A1), Vaderoarna (VA), Helgoland North (HN), Fino-1 (F1), Fino-3 (F3), Sleipner-A (SA), and Ekofisk (EK) during the two winter storms in RUNE project. Observations are shown in black dots, modeled H_{m0} using different source terms are shown in colored solid lines, and the corresponding colored dotes show the absolute error between modeled results and observations.

One-dimensional wave spectrum during the whole simulation period at RUNE site is presented in Figure 8. The colored lines in Figure 8a shows the data from buoy measurements, and the black envelop lines are used to mark the upper and lower bound of the measurement data. The colored lines in Figure 8b, 8c, and 8d are from SWAN simulations using KOM, JANS,

10   and WBLM source terms, and the black envelop lines are the same as in Figure 8a. The three simulations generally capture the shape of the measured spectrum. In comparison with the measurements, KOM and JANS tend to overestimate the energy

Table 6. Statistics of simulated significant wave height (H_{m0}) in comparison with measurements at Fjaltring (FG), Hanstholm (HM), A121 (A1), Vaderoarna (VA), Helgoland North (HN), Fino-1 (F1), Fino-3 (F3), Sleipner-A (SA), and Ekofisk (EK) from 2015-11-28 to 2015-12-08. The statistics include mean difference (BIAS), root mean square difference (RMSE), and scatter index (SI). In each column, the values of smallest absolute errors are signed with bold text.

Statistics	Exp.	FG	HM	SA	EK	F1	F3	A1	VA	HN
BIAS	KOM	**0.01**	-0.07	**-0.12**	-0.12	0.06	**-0.01**	-0.14	-0.25	-0.15
	JANS	-0.06	-0.08	-0.27	-0.12	**0.02**	-0.08	-0.22	-0.32	-0.26
	WBLM	0.13	**0.00**	-0.19	**-0.06**	0.09	**-0.01**	**-0.08**	**-0.11**	**-0.13**
RMSE	KOM	0.64	0.54	**0.51**	0.54	0.49	0.51	0.47	0.69	0.60
	JANS	0.57	0.52	0.56	0.60	0.51	0.54	0.48	0.72	0.66
	WBLM	**0.51**	**0.43**	0.52	**0.53**	**0.37**	**0.41**	**0.36**	**0.67**	**0.57**
SI	KOM	0.19	0.20	**0.14**	**0.17**	0.17	0.17	0.13	**0.17**	0.16
	JANS	0.17	0.20	**0.14**	0.19	0.18	0.18	0.12	**0.17**	0.17
	WBLM	**0.14**	**0.17**	**0.14**	**0.17**	**0.13**	**0.14**	**0.10**	**0.17**	**0.15**

around the spectral peak while WBLM gives better energy estimation around the spectral peak. Both KOM and JANS show a level-off of energy at frequencies higher than about 0.3 Hz while the measurement and WBLM do not, which may explain the failure of KOM and JANS in simulating T_{m01}. However, seemingly WBLM tends to overestimate the energy at frequencies higher than the peak, which needs further investigations.

5 Discussion

This study first calibrates the WBLM wind-input and dissipation source terms in idealized fetch-limited cases, and further validates the model in idealized depth-limited cases and two real storm cases. In the selected cases, it is proven that the revised WBLM source terms can be used for real cases, and can provide certain wave properties better than the original ones in SWAN, such as KOM and JANS. However, two storm cases do not represent all the wave conditions in the ocean, e.g. bimodal waves, slant waves, and swells are not analyzed in detail in this study. Therefore, more comprehensive analysis and validations from different data resources such as satellite data are still necessary in further studies.

The main difference between WBLM and previous wind-input source functions in SWAN is that the WBLM explicitly considers physics such as the growth rate reduction of short wind waves in the presents of long waves. This effect mainly affect the young waves. Moreover, the modification of the dissipation coefficient is also focus on the young wind waves. Therefore, the introduction of WBLM source terms to SWAN mainly improves the young wind waves which are usually found in the coastal areas. This can be seen in Figure 7. The significant wave height (H_{m0}) at the storm peak in the open sea sites, including A121 (Figure 7c), Sleipner-A (Figure 7h), and Ekofisk (Figure 7i) are underestimated by WBLM in comparison with measurements, while in the other coastal sites, the H_{m0} at the storm peak are captured quite well by WBLM. Relating the underestimation of
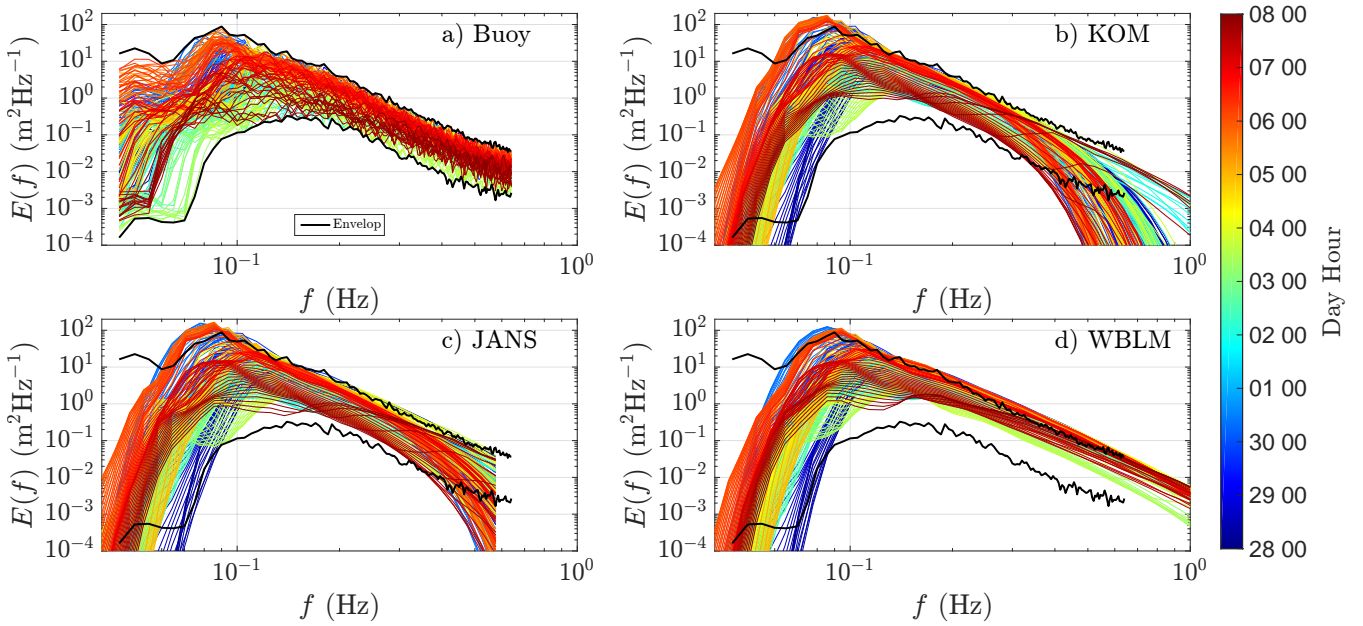
Figure 8. One-dimensional wave spectrum from buoy measurement at RUNE with all available data during the two storms (a), (b-d) are simulated with different source terms. The color of the lines represent different time. The black solid lines on each panel are the envelop lines to mark the upper and lower bound of the measurement data.

H_{m0} at the storm peak in the open sea sites and the underestimation of T_p at RUNE (Figure 6e), these defects maybe due to the inaccuracy of the calculation of nonlinear four wave interactions in low frequencies or the overestimation of swell dissipation. Here we simply added a positive wave age tuning parameter α in equation 11 following Bidlot et al. (2007) to shifts the wave growth towards lower frequency, which may not enough to overcome these defects. A more exact method for the calculation

5 of nonlinear four wave interactions and an independent swell dissipation such as Ardhuin et al. (2010) is needed in the future study.

As mentioned in Du et al. (2017), one of the biggest strengths of WBLM is in the estimation of the air-sea momentum flux. Since this study mainly concerns its behavior in the wave simulations, the air-sea momentum flux (or roughness length / drag coefficient) is not included in the analysis. A future study with the focus on its momentum flux estimation was carried out and

10 presented in Du (2017) Chapter 8, and it was found that the WBLM method provides reliable roughness length estimation in terms of the magnitude and the spatial distribution of it in coastal shallow water in comparison with point measurements and the Envisat ASAR backscatter.

The WBLM source terms is found to improve the prediction of the mean period significantly. Through analyzing the frequency spectra, it is speculated to be caused by an improved description of the high frequency part of the spectrum. However,

15 the energy from WBLM in high frequencies seems too high in comparison with measurements. Therefore, the energy distribution in high frequency range needs to be further investigated. One possible way of reducing this overestimated energy in high

frequencies is by tuning the parameters in the cumulative dissipation source function (e.g. C_{cu} in equation 19). However, the tuning of these parameters have to be followed by the tuning of the other parameters in the source terms including wind-input, white-capping, nonlinear four wave interactions, etc to make sure that both the stress estimation and the wave simulation are all satisfied.

5   Janssen (1991)'s wind-input source function was found by Du et al. (2017) and Du (2017) Chapter 5 to be wrongly implemented in SWAN. We found that in the calculation of the contribution of high frequency tail to wave stress code, the judgment of whether the growth rate coefficient of a frequency (β_g) over all directions is zero, is called before calculating β_g in all the directions. This may disregard some of the high frequency waves and therefore reduces the calculated wave stress. We also tried our best to change the code following the description of Bidlot et al. (2007) and by implementing some functions from

10 WAM code (https://github.com/mywave/WAM) to SWAN. Since this study is mainly focus on the usage of WBLM, a detailed analysis of Janssen implementation in SWAN is out of the scope of this paper.

6   Conclusions

This study aims at applying the WBLM source functions of Du et al. (2017) in SWAN for real wave simulations. Several improvements on the WBLM wind-input and white-capping dissipation source functions are realized. Firstly, the WBLM

15 wind-input source function is modified by considering the wind profile change in the estimation of the non-dimensional critical height. Secondly, a revised white-capping dissipation source function is applied which enables the WBLM method being used for varying wind conditions. Thirdly, a few refinements on the numerical algorithms of WBLM in SWAN are done to improve the model stability and efficiency, which make it possible to be used for large domain and high resolution simulations.

    The new pair of WBLM wind-input and dissipation source function is calibrated with fetch-limited and depth-limited simu-

20 lations. It is proven to be able to reproduce the benchmark wave growth curve of Kahma and Calkoen (1992), the energy level and the one-dimensional wave spectrum measured by Young and Babanin (2006b) in the depth-limited study.

    The WBLM wind-input and dissipation source functions are validated with several point measurements during two storms over the North Sea. Results show that in comparison with the original wind-input and dissipation source functions in SWAN, namely Komen et al. (1984) and Janssen (1991), WBLM improves the prediction of significant wave height and mean wave

25 period in comparison with measurements.

Code and data availability. The source code for SWAN used in this study is freely available at http:// swanmodel.sourceforge.net. The bathymetry data is obtained from EMODnet (http://www.emodnet-bathymetry.eu/). The observational wave data is downloaded from NOOS (https://noos.bsh.de/), FINO (http://fino.bsh.de), and eKlima (http://sharki.oslo.dnmi.no). CFSR 10 m wind speed is download from https://rda .ucar.edu/datasets/ds093.1/. The model data and source code modifications can be achieved from the corresponding author.

Appendix A: D85 and JONSWAP spectra

The D85 (Donelan et al., 1985) spectra is described by:

$$E(f) = \alpha_D \frac{g^2}{(2\pi)^4} f_p^{-1} f^{-4} exp\left[-\left(\frac{f}{f_p}\right)^{-4}\right] \cdot \gamma_D^{exp\left[\frac{-(f-f_p)^2}{2\sigma_D^2 f_p^2}\right]}, \tag{A1}$$

where f is the frequency and f_p is the frequency at the spectral peak. α_D is a equilibrium range parameter which is written as:

$$\alpha_D = 0.006 \left(\frac{U_{10}}{c_p}\right)^{0.55}, \tag{A2}$$

where U_{10} is 10 m wind speed. c_p is the phase velocity at the spectral peak. In deep water condition, $c_p = \frac{g}{2\pi f_p}$, where g is the gravity acceleration. γ_D is a peak enhancement factor:

$$\gamma_D = MAX\left[1.7 + 6.0\log\left(\frac{U_{10}}{c_p}\right), 1.7\right], \tag{A3}$$

σ_D is a peak width parameter, which is written as:

$$\sigma_D = 0.008\left[1 + 4\left(\frac{U_{10}}{c_p}\right)^{-3}\right], \tag{A4}$$

The JONSWAP (Hasselmann et al., 1973) spectra is described by:

$$E(f) = \alpha_J \frac{g^2}{(2\pi)^4} f^{-5} exp\left[-\frac{5}{4}\left(\frac{f}{f_p}\right)^{-4}\right] \cdot \gamma_J^{exp\left[\frac{-(f-f_p)^2}{2\sigma_J^2 f_p^2}\right]} \tag{A5}$$

where the equilibrium range parameter it is written as:

$$\alpha_J = 0.076\widetilde{x}^{-0.22}, \tag{A6}$$

where $(\widetilde{x} = xg/U_{10}^2)$ is a non-dimensional fetch, and x is the fetch. Parameterization for the peak enhancement factor (γ_J) for JONSWAP spectra is not provided by Hasselmann et al. (1973). According to Hasselmann et al. (1973), γ_J is scatted between 1.5 to 6.0, with an average value of 3.3. So we use the same equation as D85 (equation A3) with a limit of $1.5 \leq \gamma_J \leq 6.0$. The peak width parameter is written as:

$$\sigma_J = \begin{cases} 0.07; f < f_p \\ 0.09; f \geq f_p. \end{cases} \tag{A7}$$

For both D85 and JONSWAP spectrum, the peak frequency (f_p) for a given wind speed (U_{10}) and fetch (x) is calculated from the fetch-limited wave growth relationship of Kahma and Calkoen (1992):

$$f_p = 2.1804\widetilde{x}^{-0.27} \cdot \frac{g}{U_{10}}. \tag{A8}$$

Appendix B: Definition of statistics

Take X as observation value and Y as modeled value, the mean difference is defined as:

$$BIAS = \frac{1}{N} \sum_{i=1}^{N} (Y - X)_i.$$ (B1)

The root mean square difference is defined as:

$$RMSE = \sqrt{\frac{1}{N} \sum_{i=1}^{N} (Y - X)_i^2}.$$ (B2)

The scatter index is defined as:

$$SI = \frac{\sqrt{\frac{1}{N} \sum_{i=1}^{N} (Y - X - BIAS)_i^2}}{\frac{1}{N} \sum_{i=1}^{N} |X_i|}.$$ (B3)

5   *Acknowledgements.* This project has received funding from the Danish Forskel project X-WiWa (PSO-12020), the European Union's H2020 Programme for Research, Technological Development and Demonstration under Grant Agreement No: H2020-EO-2016-730030- CEASE-LESS, and the National Key Research and Development Program of China, 2017YFC1404200. We are grateful to Jean Raymond Bidlot from ECMWF, Anna Rutgersson from Uppsala University, and Henrik Bredmose from DTU Wind Energy for helpful discussions and inputs. Furthermore, we would like to thank Rogier Floors from DTU Wind Energy for providing the measurement data during Danish ForskEL project
10   RUNE (12263).

References

Alves, J. H. G. M. and Banner, M. L.: Performance of a Saturation-Based Dissipation-Rate Source Term in Modeling the Fetch-Limited Evolution of Wind Waves, Journal of Physical Oceanography, 33, 1274–1298, https://doi.org/10.1175/1520-0485(2003)033<1274:POASDS>2.0.CO;2, 2003.

5 Ardhuin, F.: Dissipation parameterizations in spectral wave models and general suggestions for improving on today's wave models Fabrice Ardhuin e, in: ECMWF Workshop on Ocean Waves, June, pp. 113–124, 2012.

Ardhuin, F. and Roland, A.: Coastal wave reflection, directional spread, and seismoacoustic noise sources, Journal of Geophysical Research: Oceans, 117, 1–16, https://doi.org/10.1029/2011JC007832, 2012.

Ardhuin, F., Rogers, E., Babanin, A. V., Filipot, J.-F., Magne, R., Roland, A., van der Westhuysen, A., Queffeulou, P., Lefevre, J.-M., Aouf,
10 L., and Collard, F.: Semiempirical Dissipation Source Functions for Ocean Waves. Part I: Definition, Calibration, and Validation, Journal of Physical Oceanography, 40, 1917–1941, https://doi.org/10.1175/2010JPO4324.1, 2010.

Ardhuin, F., Roland, A., Dumas, F., Bennis, A.-C., Sentchev, A., Forget, P., Wolf, J., Girard, F., Osuna, P., and Benoit, M.: Numerical wave modelling in conditions with strong currents: dissipation, refraction and relative wind, Journal of Physical Oceanography, p. 120723054131002, https://doi.org/10.1175/JPO-D-11-0220.1, 2012.

15 Babanin, A. V. and Young, I. R.: Two-phase behaviour of the spectral dissipation of wind waves, in: Proc. Ocean Waves Measurements and Analysis, Fifth Intern. Symposium WAVES2005, December 2016, 2005.

Babanin, A. V., Tsagareli, K. N., Young, I. R., and Walker, D. J.: Numerical Investigation of Spectral Evolution of Wind Waves. Part II: Dissipation Term and Evolution Tests, Journal of Physical Oceanography, 40, 667–683, https://doi.org/10.1175/2009JPO4370.1, 2010.

Banner, M. L. and Morison, R. P.: Refined source terms in wind wave models with explicit wave breaking prediction. Part I: Model framework
20 and validation against field data, Ocean Modelling, 33, 177–189, https://doi.org/10.1016/j.ocemod.2010.01.002, 2010.

Battjes, J. A. and Janssen, J. P. F. M.: Energy loss and set-up due to breaking of random waves, in: Proceedings of 16th International Conference on Coastal Engineering, Am. Soc. of Civ. Eng., New York, pp. 569–587, American Society of Civil Engineers, New York, NY, https://doi.org/10.1017/CBO9781107415324.004, 1978.

Bidlot, J.-R.: Present Status of Wave Forecasting at E . C . M . W . F ., in: ECMWF Workshop on Ocean Waves, 2012.

25 Bidlot, J.-R., Janssen, P. A. E. M., and Abdalla, S.: A revised formulation of ocean wave dissipation and its model impact., ECMWF Technical Memorandum, 509, http://www.citeulike.org/group/11419/article/6354018, 2007.

Bolaños, R.: D3 . 3 Metocean Conditions and Wave Modelling, Tech. Rep. November, 2016.

Bolaños, R. and Rørbæk, K.: D3 . 1 Metocean Buoy Deployment, Tech. Rep. November, 2016.

Bolaños, R., Larsén, X. G., Petersen, O., Nielsen, J., Kelly, M., Kofoed-Hansen, H., Du, J., Sørensen, O., Larsen, S., Hahmann, A., and
30 Badger, M.: Coupling atmospherere and waves for coastal wind turbine design, Proceedings of the Coastal Engineering Conference, 2014-Janua, 1–11, 2014.

Booij, N., Ris, R., and Holthuijsen, L.: A third-generation wave model for coastal regions. I- Model description and validation, Journal of geophysical research, 104, 7649–7666, https://doi.org/10.1029/98JC02622, 1999.

Cavaleri, L.: Wave Modeling—Missing the Peaks, Journal of Physical Oceanography, 39, 2757–2778,
35 https://doi.org/10.1175/2009JPO4067.1, 2009.

Cavaleri, L., Alves, J. H. G. M., Ardhuin, F., Babanin, A., Banner, M., Belibassakis, K., Benoit, M., Donelan, M., Groeneweg, J., Herbers, T. H. C., Hwang, P., Janssen, P. A. E. M., Janssen, T., Lavrenov, I. V., Magne, R., Monbaliu, J., Onorato, M., Polnikov, V., Resio, D., Rogers,

W. E., Sheremet, A., McKee Smith, J., Tolman, H. L., van Vledder, G., Wolf, J., and Young, I.: Wave modelling - The state of the art, Progress in Oceanography, 75, 603–674, https://doi.org/10.1016/j.pocean.2007.05.005, 2007.

Donelan, M. A., Hamilton, J., and Hui, W. H.: Directional Spectra of Wind-Generated Waves, Philosophical Transactions of the Royal Society of London. Series A. Mathematical and Physical Sciences, 315, 509–562, https://doi.org/10.1098/rsta.1985.0054, 1985.

5 Du, J.: Coupling atmospheric and ocean wave models for storm simulation, Ph.D. thesis, Technical University of Denmark, https://doi.org/10.11581/DTU:00000020, 2017.

Du, J., Bolaños, R., and Larsén, X.: The use of a wave boundary layer model in SWAN, Journal of Geophysical Research: Oceans, pp. 1063–1084, https://doi.org/10.1002/2016JC012104, 2017.

Floors, R., Hahmann, A., Peña, A., and Karagali, I.: Estimating near-shore wind resources E-Report DTU Wind Energy, vol. 0116, 2016a.

10 Floors, R., Lea, G., Peña, A., Karagali, I., and Ahsbahs, T.: Report on RUNE's coastal experiment and first inter-comparisons between measurements systems, vol. 0115, 2016b.

Floors, R., Peña, A., Lea, G., Vasiljevic, N., Simon, E., and Courtney, M.: The RUNE experiment-A database of remote-sensing observations of near-shore winds, Remote Sensing, 8, https://doi.org/10.3390/rs8110884, 2016c.

G. J. Komen, L. Cavaleri, M. Donelan, K. Hasselmann, S. Hasselmann, and Janssen, P. A. E. M.: Dynamics and modelling of ocean waves, https://doi.org/10.1017/CBO9780511628955, 1994.

15 Hasselmann, K.: On the spectral dissipation of ocean waves due to white capping, Boundary-Layer Meteorology, 6, 107–127, https://doi.org/10.1007/BF00232479, 1974.

Hasselmann, K., Barnett, T. P., Bouws, E., Carlson, H., Cartwright, D. E., Enke, K., Ewing, J. A., Gienapp, H., Hasselmann, D. E., Kruseman, P., Meerburg, A., Muller, P., Olbers, D. J., Richter, K., Sell, W., and Walden, H.: Measurements of Wind-Wave Growth and Swell Decay

20 during the Joint North Sea Wave Project (JONSWAP), Ergnzungsheft zur Deutschen Hydrographischen Zeitschrift Reihe, A(8), p.95, https://doi.org/citeulike-article-id:2710264, 1973.

Hua, F. and Yuan, Y.: Theoretical Study of Breaking Wave Spectrum and its Application, in: Breaking Waves, pp. 277–282, Springer Berlin Heidelberg, Berlin, Heidelberg, https://doi.org/10.1007/978-3-642-84847-6-30, 1992.

Janssen, P. a. E. M.: Quasi-linear Theory of Wind-Wave Generation Applied to Wave Forecasting, Journal of Physical Oceanography, 21,

25 1631–1642, https://doi.org/10.1175/1520-0485(1991)021<1631:QLTOWW>2.0.CO;2, 1991.

Kahma, K. K. and Calkoen, C. J.: Reconciling Discrepancies in the Observed Growth of Wind-generated Waves, https://doi.org/10.1175/1520-0485(1992)022<1389:RDITOG>2.0.CO;2, 1992.

Komen, G. J., Hasselmann, K., and Hasselmann, K.: On the Existence of a Fully Developed Wind-Sea Spectrum, Journal of Physical Oceanography, 14, 1271–1285, https://doi.org/10.1175/1520-0485(1984)014<1271:OTEOAF>2.0.CO;2, 1984.

30 Komen, G. J., Cavareli, L., Donelan, M., Hasselmann, K., Hasselmann, S., and Janssen, P. A. E. M.: Dynamics and modelling of ocean waves, Cambridge University Press, 1994.

Larsén, X. G., Du, J., Bolaños, R., and Larsen, S.: On the impact of wind on the development of wave field during storm Britta, Ocean Dynamics, 67, 1407–1427, https://doi.org/10.1007/s10236-017-1100-1, 2017.

Leckler, F., Ardhuin, F., Filipot, J. F., and Mironov, A.: Dissipation source terms and whitecap statistics, Ocean Modelling, 70, 62–74,

35 https://doi.org/10.1016/j.ocemod.2013.03.007, 2013.

Longuet-Higgins, M. S.: On Wave Breaking and the Equilibrium Spectrum of Wind-Generated Waves, Proceedings of the Royal Society A: Mathematical, Physical and Engineering Sciences, 310, 151–159, https://doi.org/10.1098/rspa.1969.0069, 1969.

Melville, W. K. and Matusov, P.: Distribution of breaking waves at the ocean surface., Nature, 417, 58–63, https://doi.org/10.1038/417058a, 2002.

Miles, J. W.: On the generation of surface waves by shear flows. Part 2, Journal of Fluid Mechanics, 3, 568–582, https://doi.org/10.1017/S0022112059000830, 1957.

5   Phillips, O. M.: Spectral and statistical properties of the equilibrium range in wind-generated gravity waves, Journal of Fluid Mechanics, 156, 505–531, https://doi.org/https://doi.org/10.1017/S0022112085002221, 1985.

Polnikov, V. G.: On a description of a wind-wave energy dissipation function, in: The Air–Sea Interface: Radio and Acous- tic Sensing, Turbulence and Wave Dynamics, edited by Donelan, M. A., Hui, W. H., and Plant, W. J., pp. 277–282, Rosenstiel School of Marine and Atmospheric Science, University of Miami, 1993.

10   Snyder, R. L., Dobson, F. W., Elliott, J. A., and Long, R. B.: Array measurements of atmospheric pressure fluctuations above surface gravity waves, Journal of Fluid Mechanics, 102, 59, https://doi.org/10.1017/S0022112081002528, 1981.

Sørensen, O. R., Kofoed-Hansen, H., Rugbjerg, M., and Sørensen, L. S.: A third-generation spectral wave model using an unstructured finite volume technique, Proceedings of the 29th Intern. Conf. on Coastal Eng., pp. 894–906, https://doi.org/10.1142/9789812701916-0071, 2004.

15   SWAN: Swan Scientific and Technical Documentation, SWAN Cycle III version 41.01, pp. 1–132, 2014.

Tolman, H. L. and Chalikov, D.: Source Terms in a Third-Generation Wind Wave Model, https://doi.org/10.1175/1520-0485(1996)026<2497:STIATG>2.0.CO;2, 1996.

van der Westhuysen, A. J., Zijlema, M., and Battjes, J. A.: Nonlinear saturation-based whitecapping dissipation in SWAN for deep and shallow water, Coastal Engineering, 54, 151–170, https://doi.org/10.1016/j.coastaleng.2006.08.006, 2007.

20   Young, I. R. and Babanin, A. V.: Spectral Distribution of Energy Dissipation of Wind-Generated Waves due to Dominant Wave Breaking, Journal of Physical Oceanography, 36, 376–394, https://doi.org/10.1175/JPO2859.1, 2006a.

Young, I. R. and Babanin, A. V.: The form of the asymptotic depth-limited wind wave frequency spectrum, Journal of Geophysical Research: Oceans, 111, 1–15, https://doi.org/10.1029/2005JC003398, 2006b.

Young, I. R., Banner, M. L., Donelan, M. A., Babanin, A. V., Melville, W. K., Veron, F., and McCormick, C.: An integrated sys-
25   tem for the study of wind-wave source terms in finite-depth water, Journal of Atmospheric and Oceanic Technology, 22, 814–831, https://doi.org/10.1175/JTECH1726.1, 2005.

Yuan, Y., Tung, C. C., and Huang, N. E.: Statistical Characteristics of Breaking Waves, in: Wave Dynamics and Radio Probing of the Ocean Surface, pp. 265–272, Springer US, Boston, MA, https://doi.org/10.1007/978-1-4684-8980-4-18, 1986.

Zieger, S., Babanin, A. V., Erick Rogers, W., and Young, I. R.: Observation-based source terms in the third-generation wave model WAVE-
30   WATCH, Ocean Modelling, 96, 2–25, https://doi.org/10.1016/j.ocemod.2015.07.014, 2015.

Zijlema, M., Van Vledder, G. P., and Holthuijsen, L. H.: Bottom friction and wind drag for wave models, Coastal Engineering, 65, 19–26, https://doi.org/10.1016/j.coastaleng.2012.03.002, 2012.